buildings

MDPI

Article

Improvement of Latent Heat Thermal Energy Storage Rate for Domestic Solar Water Heater Systems Using Anisotropic Layers of Metal Foam

Obai Younis [1], Masoud Mozaffari [2], Awadallah Ahmed [3] and Mehdi Ghalambaz [4,*]

[1] Department of Mechanical Engineering, College of Engineering in Wadi Alddawasir, Prince Sattam Bin Abdulaziz University, Wadi Addawaser 11991, Saudi Arabia; o.elamin@psau.edu.sa
[2] Department of Mechanical Engineering, Najafabad Branch, Islamic Azad University, Najafabad 85141-43131, Iran; masoodmozafari66@yahoo.com
[3] Department of Mechanical Engineering, Faculty of Engineering and Technology, Nile Valley University, Atbara 46611, Sudan; awadallahahmed985@gmail.com
[4] Institute of Research and Development, Duy Tan University, Da Nang 550000, Vietnam
* Correspondence: mehdighalambaz@duytan.edu.vn

Abstract: Latent Heat Transfer Thermal Energy Storage (LHTES) units are crucial in managing the variability of solar energy in solar thermal storage systems. This study explores the effectiveness of strategically placing layers of anisotropic and uniform metal foam (MF) within an LHTES to optimize the melting times of phase-change materials (PCMs) in three different setups. Using the enthalpy–porosity approach and finite element method simulations for fluid dynamics in MF, this research evaluates the impact of the metal foam's anisotropy parameter (Kn) and orientation angle (ω) on thermal performance. The results indicate that the configuration placing the anisotropic MF layer to channel heat towards the lower right corner shortens the phase transition time by 2.72% compared to other setups. Conversely, the middle setup experiences extended melting periods, particularly when ω is at 90°—an increase in Kn from 0.1 to 0.2 cuts the melting time by 4.14%, although it remains the least efficient option. The findings highlight the critical influence of MF anisotropy and the pivotal role of ω = 45°. Angles greater than this significantly increase the liquefaction time, especially at higher Kn values, due to altered thermal conductivity directions. Furthermore, the tactical placement of the anisotropic MF layer significantly boosts thermal efficiency, as evidenced by a 13.12% reduction in the PCM liquefaction time, most notably in configurations with a lower angle orientation.

Keywords: Sustainability; clean energy; building energy storage; building hot water; anisotropic copper metal foam; phase-change material

Citation: Younis, O.; Mozaffari, M.; Ahmed, A.; Ghalambaz, M. Improvement of Latent Heat Thermal Energy Storage Rate for Domestic Solar Water Heater Systems Using Anisotropic Layers of Metal Foam. *Buildings* **2024**, *14*, 2322. https://doi.org/10.3390/buildings14082322

Academic Editor: Zhenjun Ma

Received: 18 June 2024
Revised: 22 July 2024
Accepted: 23 July 2024
Published: 26 July 2024

1. Introduction

The surge in global energy demand, driven by contemporary lifestyles, has considerably intensified the focus on developing innovative clean energy technologies. In response, the United Nations Organization has put forth 17 sustainable development goals, with notable objectives including ensuring accessible, cost-effective, sustainable, and innovative energy for all (Goal 7) and promoting the development of resilient, secure, and sustainable urban areas (Goal 11). These efforts are crucial for addressing the pressing challenges of energy sustainability. Heat Thermal Energy Storage (LHTES), an advancement in this field, employs phase-change materials (PCMs) to hold and discharge thermal energy in response to temperature shifts [1]. LHTES systems can also shift electrical power consumption. For instance, by storing cooling energy during off-peak hours and releasing it during peak demand, LHTES effectively shifts the energy load, enhancing the efficiency of cooling operations and reducing energy waste [2]. With an appropriate design, the PCM can help lower costs and achieve energy savings in buildings while ensuring a comfortable indoor environment [3].

While LHTES systems provide a promising solution for aligning energy supply with growing demand, their efficiency is often restricted by the low thermal properties of PCMs [1,4]. To improve the heat transfer in LHTES systems, researchers have explored several methods to enhance LHTES thermal performance, such as integrating fins [5–8], nano additives [9–11], rotation-based methods [12,13], and porous media, applied either alone or in combination [14].

LHTES technologies, particularly using PCMs, are crucial for enhancing building energy efficiency. Experimental tests [15] were carried out on the thermophysical properties of three medium-temperature PCMs, OM65, OM55, and RT55, for use in hot water and heating systems in building applications. The results confirm that these PCMs can substantially reduce energy consumption and increase efficiency. Chen's study [16] discovered the use of MF/stearic acid composite PCMs in LHTES units for buildings, exhibiting that a 50% MF filling in an L-configuration increased the thermal storage rate density by 7.1% and reduced costs by 50%. This configuration enhanced the melting rate by 11.25% compared to traditional methods. Ahmed Said et al. [17] showed that optimizing the configuration of shell-and-tube systems can significantly improve PCM melting times, boosting the system's energy storage capacity. Similarly, Boujelbene et al. [18] demonstrated that incorporating arc-shaped fins in triplex-tube TES units can reduce solidification times by 75% and increase heat recovery rates by 284%, enhancing thermal responsiveness. Moreover, Kabore's study [19] utilized vortex generators in a shell-and-tube LHTES unit with PT23 as the PCM, boosting convective heat transfer. The optimized configurations in the study expedited PCM melting/solidifying kinetics by more than 110%, showcasing potential improvements in thermal comfort for buildings. M'hamdi [20] simulated PCM mortar in buildings across two Moroccan climates and showed an 11% reduction in energy load for cooling and heating. These innovations are essential for effectively integrating renewable energy sources into building management systems and promoting energy sustainability.

Recently, porous media, in particular, has received substantial attention for its potential to boost the thermal efficiency of LHTES units. Research by Xu et al. [21] demonstrated that specific structural configurations involving porous media could greatly reduce melting times by as much as 43.1%. Subsequently, Yang et al. [22] designed an LHTES system incorporating graded metal foam (MF) and fins, which not only shortened melting times by 27.23%, but also improved thermal energy storage rates by 36.52% compared to using graded MF alone. Huang's [23] research reported that PCMs with a porous lattice structure in building walls reduced the internal panel temperature by 15% and enhanced PCM melting rates by up to 53.1%, underscoring the efficiency of this approach for thermal management in buildings. In an innovative study, Iasiello et al. [24] both empirically and numerically assessed aluminum foams with varying porosities and pores per inch (PPI) to carefully study the melting front in MF/PCM composites. Their outcomes suggested that reduced porosity diminished the melting time, while PPI had minimal impact.

Furthermore, investigations have highlighted diverse enhancements in LHTES performance. Chibani et al. [25] showed that systems combining MF with PCMs outperformed traditional nano-enhanced PCMs in terms of melting performance. Additional studies indicated that employing radial-graded and circumferential-graded structures could effectively alleviate issues of non-uniform melting and slow melting rates [26]. The development of innovative materials also plays a role in advancing LHTES technology. In one study [27], inserting anisotropic woven metal fibers into PCMs developed heat transfer, improving energy storage rates by 40%. Curved fibers outperformed at high porosity, while straight fibers were better at lower porosity, highlighting the advantages of anisotropic over isotropic porous media in LHTES applications. In their research, Liu et al. [28] enhanced thermal conductivity using porous AIN ceramics, leading to greater energy densities in LHTES designs. They reported thermal conductivity values of between 31.8 and 52.63 W/m.K, and found an increase in solar absorptance from 70% to 90%. Research [29] modeled wavy channel geometries in LHTES units for building floors, showing that step-function

geometry reduced PCM discharge time by 65.1% and increased heat recovery by 147.9%, improving thermal management.

Parallel research involving heat pipe MF [30] and various porosity copper foams [31] further underscored the importance of material properties and structural configurations in optimizing thermal storage and retrieval processes. Lei et al. observed a significant growth in thermal performance for LHTES when using paraffin combined with copper foams, achieving a 73.7% reduction in the solid-to-liquid time compared with PCM only. Using varying porosity in copper foams also reduced the average heat flux density by 4.26% and total melting time by 6.78% compared to fixed porosity. Comparative studies have also provided valuable insights into the performance of different enhancements within LHTES systems. Research in [32] revealed that fin-embedded PCM configurations have a higher melting rate, increasing by 66.67% compared with MF-embedded PCM. However, MF-embedded systems achieved a 29.41% higher solidification rate than the fin-embedded PCM. Hybrid approaches integrating MF with nano additives, as researched in [33], dramatically shortened both charging and discharging times, showcasing the synergistic benefits of combining different technologies. These times were reduced by 96.11% and 96.23%, respectively.

Additional research has focused on reducing the weight and optimizing the design of MFs used in LHTES units. Ghalambaz et al. [34] explored novel geometric designs of MFs to ameliorate thermal performance, while another study [35] found that gradient porosity in MFs could sharply decrease melting durations and provide a more uniform temperature distribution. A recent investigation on cascaded LHTES units using composite PCM and MF emphasized the crucial role of porous media's porosity in influencing the rate of energy charging and discharging [36]. Zhang et al. [37] conducted an important comparative analysis between the use of fins and MFs, affirming that MFs are still the preferred option for enhancing thermal performance in LHTES units. The key finding is that MFs remain the primary enhancer in LHTES systems. The studies briefly mentioned earlier provide a snapshot of recent research involving MFs and other technologies for enhancing LHTES performance. For more comprehensive details, refer to the reviews listed in references [38–42].

Despite these advancements, a considerable research gap remains in the strategic optimization of anisotropic and uniform MF layers within LHTES configurations, particularly in understanding how anisotropy parameters and angles affect melting duration. This gap limits the efficiency and effectiveness of LHTES designs. The current paper addresses this deficiency by exploring the impacts of anisotropy parameters and angles on melting time in LHTES systems, thereby contributing to developing thermal energy storage solutions aligned with global sustainability goals.

2. Model Description

An illustrated example of a concentrated solar heating system underscores the importance of Latent Heat Thermal Energy Storage (LHTES) in enhancing solar energy applications. Given the sporadic nature of solar energy, influenced by weather and timing, LHTES proves vital. It efficiently accumulates a significant energy quantity at the melting point in a reduced space, stabilizing energy outputs in solar systems prone to fluctuations. The setup includes components such as a solar collector, an LHTES unit, a hot water storage tank, and circulating pumps. In this configuration, the collector warms the water, which is then conserved as sensible heat in the tank, ready to supply the building with heated water as needed. Moreover, a supplementary loop connects the storage tank to the LHTES unit. This loop is activated during times of excess heat production or reduced energy demand, enabling the pump to channel surplus heat into the LHTES. On the other hand, when solar energy production falls short, heat is drawn from the LHTES unit to compensate for the deficit, ensuring a continuous energy supply. The system's layout is depicted in Figure 1.

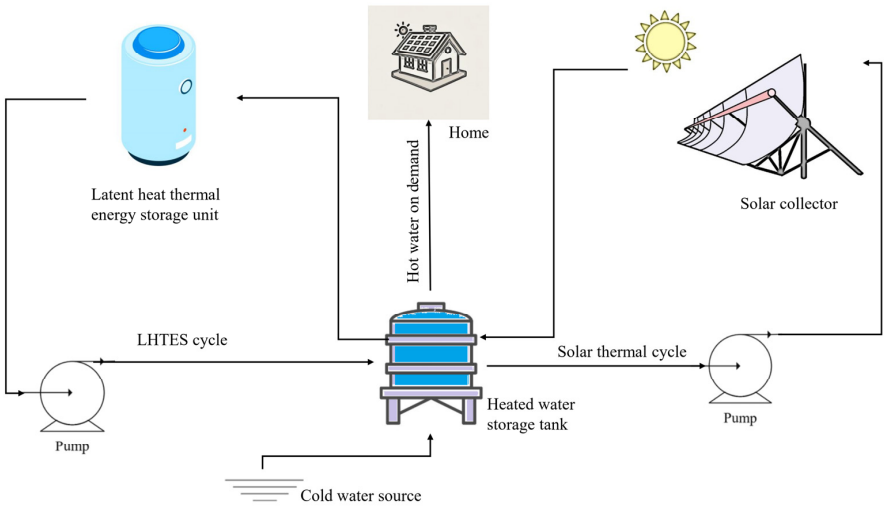

Figure 1. This diagram illustrates a solar water heating cycle featuring a latent heat thermal energy storage (LHTES) tank. Excess solar energy collected by the solar collector is transferred to the storage tank, causing it to overheat. In response, the LHTES system circulates the overheated water within its unit, allowing the heat to be absorbed by the LHTES tank. Should the temperature of the heated water tank drop significantly, the LHTES pump activates to circulate cooler water back into the LHTES unit, thereby maintaining a consistently high water temperature.

In the model presented, Figure 2 displays an LHTES tank comprising channel-shaped containers and passages for a heat transfer fluid (HTF). In this system, water circulates past the walls of the metal foam, which is made of copper, facilitating heat exchange at a temperature T_w = 339.65 K, which is higher than the PCM's melting point T_{fu}, 324.65 K. The PCM has a solidification temperature of 322.15 K and a liquefaction temperature of 327.15 K, giving a melting range of 5 K, with the average melting point considered to be 324.65 K. This induces the PCM's phase transition from solid to liquid, which absorbs substantial energy and allows for its later release during solidification, with a 15 K range. The closed square cavity is thermally insulated on all sides except for the left heated wall, measuring 15 cm $\times$ 15 cm. Figure 3 offers a closer look at the three selected configurations. It reveals two distinct MF layers designed to improve heat transfer: a uniform metal foam layer (UMFL) and an anisotropic metal foam layer (AMFL), with the AMFL strategically positioned inside the cavity. The concept of this design centers on the AMFL, which is strategically positioned to absorb heat emitted from the hot wall efficiently and redistribute it to areas with lower temperature gradients. The AMFL comprises vertical and horizontal sections, enabling a comprehensive interface with the hot wall. Specifically, the vertical section of the AMFL is designed to make full contact with the hot wall, ensuring maximal heat absorption. This absorbed heat is then conveyed through the horizontal section of the AMFL, facilitating thermal distribution across typically temperature-deprived regions. The AMFL exhibits engineered directional properties, indicated by varying thermal conductivity and permeability, based on an anisotropy parameter (Kn) and angle (ω). The orientation angle of the AMFL was systematically adjusted, ranging from a perpendicular 0° to a parallel 90° in relation to the hot wall, to evaluate its influence on the heat response of the designs. For the molten PCM, the model assumes no-slip velocity near the walls and operates under the Newtonian fluid assumption in a laminar flow regime. Additionally, the model applies the Boussinesq approximation to address the relationship between density and temperature variations in the setup. The solar collector can provide variable temperatures during the day. Such transient effects can be considered [43,44]. However, since there is a heated water tank between the solar collector and the LHTES unit, it moderates the temperature fluctuations and a constant temperature was assumed for HTF and the enclosure wall.

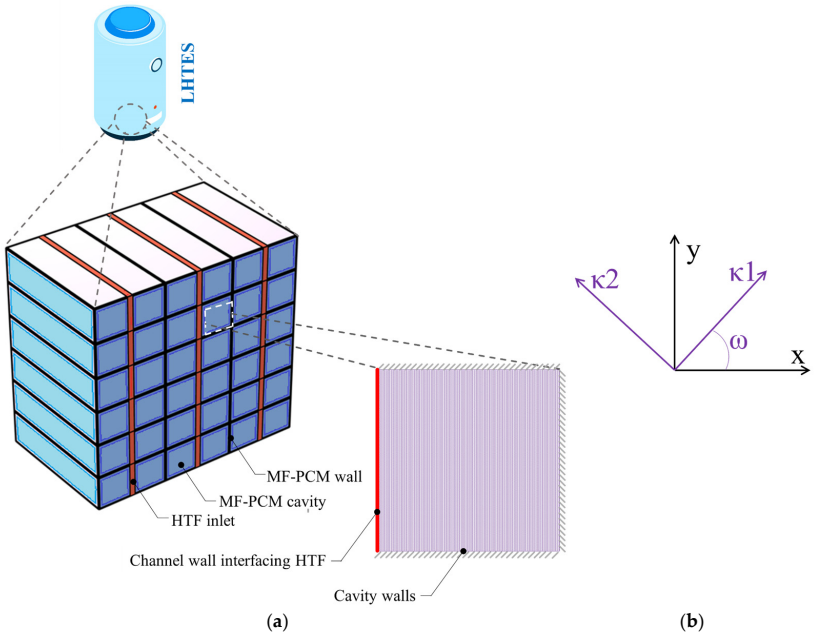

Figure 2. A two-dimensional section of a storage enclosure and a multi-channel LHTES unit. (**a**) Depiction of the storage space. (**b**) Description of the orientation related to anisotropic angles (ω). During the charging process, water flows through the heat transfer fluid (HTF) passages, maintaining high temperatures along the walls.

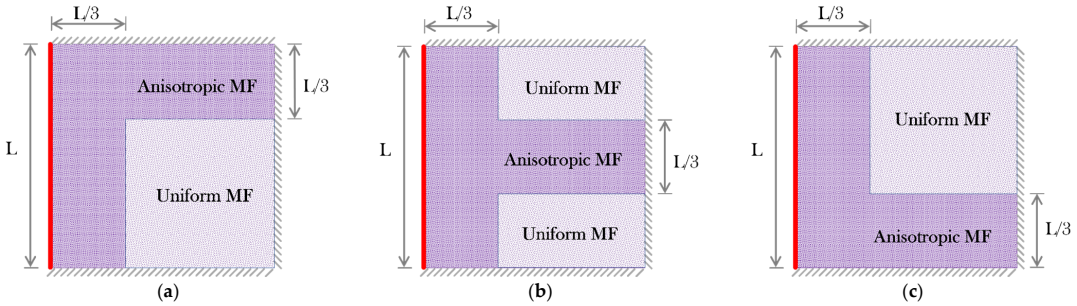

Figure 3. Schematic diagram of the MF cavity featuring a UMFL and an AMFL infused with PCM in a 2D model: (**a**) top case, (**b**) middle case, and (**c**) bottom case.

Governing Equations

The domain under investigation comprises three interlinked zones: the copper channel wall, composite uniform MF-PCM, and composite anisotropic MF-PCM. In the fusion procedure of PCMs, the continuity equation ensures mass conservation, while the momentum equation describes the melted PCM flow through the MF, considering viscous and external forces. The energy equation details how the PCM absorbs heat during the phase transition and its temperature distribution inside the MF. Using the Finite Element Method (FEM), Partial Differential Equations (PDEs), which form the basis of the governing equations conserving mass, momentum, and energy, are resolved. When combined, these equations (Equation (1)) effectively model the physical dynamics of PCM melting and movement within the MF framework. The continuity, momentum, and energy equations, respectively, are as follows [45–47]:

$$\begin{cases} \nabla.U = 0 \\ \frac{\partial U}{\partial t} + \frac{1}{\varepsilon}(U.\nabla)U = -\frac{\varepsilon}{\rho}\nabla P + \frac{\mu}{\rho}\nabla^2 U + F \\ \rho C_p \frac{DT}{Dt} = k\nabla^2 T + q_{gen} \end{cases} \quad (1)$$

The local thermal non-equilibrium (LTNE) method is deployed inside the energy transformation equation to manage heat transfer separately within each PCM and MF phase. The sections of PCM and MF are described through a set of unified governing equations, subsequently customized for individual sections by adjustments in permeability and porosity. To address the energy exchange between phases, coupling source terms are integrated. In regions of molten PCM, in uniform and anisotropic sections, natural convection is solved by the continuity and momentum equations. The enthalpy–porosity technique, which draws on a clear comparison between the semi-liquid state in the mushy zone and how fluids navigate porous media, is utilized for phase-change simulation. This approach incorporates additional source terms in the momentum equations to account for zero velocity in solid PCM based on the melt fraction (ϕ). Fluid flow in MF is modeled employing the Darcy–Brinkman–Forchheimer approach, which provides a mathematical framework in the porous medium. Hence, the expanded x-momentum equation below captures two-dimensional fluid movement through porous media, with terms adjusted to account for the porosity (ε) and the variable density (ρ_{wax}) effects. The equation also incorporates a source term that accommodates the resistance by the porous matrix and the phase change, modulating the fluid momentum due to the mushy zone characterized by the liquid fraction $\phi(T)$. The shorthand notations "*copper*", "*wax*", and "*eff*" represent, in respective order, copper MF, PCM made of paraffin, and effective characteristics in their usage. The momentum equation in the x direction is as follows [45–47]:

$$\begin{aligned}&\frac{\rho_{wax}}{\varepsilon}\left(\frac{\partial u}{\partial t}\right)+\frac{\rho_{wax}}{\varepsilon^2}\left(u\frac{\partial u}{\partial x}+v\frac{\partial u}{\partial y}\right)=-\left(\frac{\partial p}{\partial x}\right)+\frac{\mu_{wax}}{\varepsilon}\left(\frac{\partial u}{\partial x^2}^2+\frac{\partial u}{\partial y^2}^2\right)\\&-\left(\frac{\mu_{wax}}{\kappa}\right)u-\left(\rho_{wax}\frac{C_F}{\sqrt{\kappa}}|U|\right)u+\left(A_{mush}\frac{(1-\phi(T))^2}{\gamma_{mush}+\phi^3(T)}\right)u\end{aligned}\tag{2}$$

For the y-direction momentum, the corresponding momentum equation includes the same key factors and a convection heat transfer term $g\rho_{wax}\beta_{wax}(T-T_0)$, where buoyancy-driven flows are predominant during the molten PCM. The momentum equation in the y direction is as follows:

$$\begin{aligned}&\frac{\rho_{wax}}{\varepsilon}\left(\frac{\partial v}{\partial t}\right)+\frac{\rho_{wax}}{\varepsilon^2}\left(u\frac{\partial v}{\partial x}+v\frac{\partial v}{\partial y}\right)=-\left(\frac{\partial p}{\partial y}\right)+\frac{\mu_{wax}}{\varepsilon}\left(\frac{\partial v}{\partial x^2}^2+\frac{\partial v}{\partial y^2}^2\right)\\&+g\rho_{wax}\beta_{wax}(T-T_0)-\left(\frac{\mu_{wax}}{\kappa}\right)v-\left(\rho_{wax}\frac{C_F}{\sqrt{\kappa}}|U|\right)v+\left(A_{mush}\frac{(1-\phi(T))^2}{\gamma_{mush}+\phi^3(T)}\right)v\end{aligned}\tag{3}$$

Equation (4) describes energy conservation in the PCM phase. The diffusion of heat through the PCM is given by $k_{eff,wax}\nabla^2T$, while $h_v\left(T_{copper}-T_{wax}\right)$ represents the convective heat exchange involving the PCM and the surrounding copper [48]. The last term, $\varepsilon\rho_{wax}L_{wax}\frac{\partial\phi(T)}{\partial t}$, quantifies the latent heat associated with the phase-change process in the PCM. In these equations [48], effective thermal conductivities for the PCM ($k_{eff,wax}$) and the MF ($k_{eff,copper}$) are employed, displaying how pore structures impact thermal conductivities.

$$\varepsilon\left(\rho C_p\right)_{wax}\frac{\partial T_{wax}}{\partial t}+\left(\rho C_p\right)_{wax}(U.\nabla)T_{wax}=k_{eff,wax}\nabla^2T+h_v\left(T_{copper}-T_{wax}\right)-\varepsilon\rho_{wax}L_{wax}\frac{\partial\phi(T)}{\partial t}\tag{4}$$

The equation delineates the conservation of energy in the metal foam phase, where $(1-\varepsilon)(\rho C_p)_{copper}$ represents the effective heat capacity of the copper foam, adjusted for porosity (ε):

$$(1-\varepsilon)\left(\rho C_p\right)_{copper}\frac{\partial T_{copper}}{\partial t}=k_{eff,copper}\nabla^2T_{copper}+h_v\left(T_{wax}-T_{copper}\right)\tag{5}$$

In the aforementioned governing equations, several parameters are used: porous permeability (κ), the fusion latent heat (L), the Frochheimer parameter (C_F), and the thermal expansion coefficient (β). The PCM's thermophysical properties were determined through

a linear weight average calculation. In this context, the fluid of PCM and its solidified phase are shown by *l* and *s*, respectively.

$$(\rho C_p)_{wax} = \varphi(\rho C_p)_s + (1-\varphi)(\rho C_p)_l \quad (6)$$

$$\rho_{wax} = \varphi\rho_s + (1-\varphi)\rho_l \quad (7)$$

In the melting process, the Carman–Kozeny model, denoted by the term A_{mush}, is responsible for managing the velocities of PCM. This is achieved by decelerating the velocity as the melting front approaches the solid phase. Within this model, the mushy region is considered a porous medium. Transitioning from the liquid to the solid part results in a sharp drop in the medium's porosity and permeability. The fluid velocity tends towards zero, illustrating the damping effect of body force in this zone. A_{mush} serves as a constant that reflects the configuration of the melting front, with specific values assigned to regulate different scenarios: 6×10^6 Pa.s/m^2 for clear flow and a significantly higher 1×10^{10} Pa.s/m^2 in the MF region to control the flow solution in solid areas effectively. Alongside A_{mush}, a smaller constant, γ_{mush}, is also integrated, set at 0.001. This setting is crucial as it helps circumvent any instances of division by zero.

The model redefines viscosity as $\mu = (1-\phi) \times a + \mu_{wax,l}\,\phi$, with a being a deliberately high value (10^4 Pa.s). As a result, in this formula, when ϕ equals 1, the viscosity nears the usual dynamic viscosity of $\mu_{wax,l}$ in liquid regions. Conversely, when ϕ equals zero, the viscosity noticeably increases in solid domains, enhancing flow resistance. The volume fraction of melting, ϕ, varies with temperature, as described below [49]:

$$\phi(T) = \begin{cases} 0 & T < T_{fu} - \frac{\Delta T_{fu}}{2} \quad \text{(Solid } wax\text{)} \\ \frac{(T-T_{fu})}{\Delta T_{fu}} + \frac{1}{2} & T_{fu} - \frac{\Delta T_{fu}}{2} \le T \le T_{fu} + \frac{\Delta T_{fu}}{2} \quad \text{(Mushy region)} \\ 1 & T > T_{fu} + \frac{\Delta T_{fu}}{2} \quad \text{(Liquid } wax\text{)} \end{cases} \quad (8)$$

The effective thermal conductivity of the PCM was determined through an equation referenced in references [45,48].

$$k_{\text{eff, } wax} = \frac{1}{3}(2+\varepsilon)k_{wax} 0.929 < \varepsilon < 0.974 \quad (9)$$

For the AMFL's LHTES, variations in thermal conductivity and permeability are considered across various directions, a result influenced by both the anisotropic parameter (*Kn*) and the angle of anisotropy (ω). This occurs as the MF layer's ligaments are selectively reinforced in a single direction, developing thermal conductivity at the expense of permeability. To capture these unique directional properties, the model employs a second-order tensor, detailed in the equations that follow [50].

$$\kappa = \begin{bmatrix} \kappa_2(\sin\omega)^2 + \kappa_1(\cos\omega)^2 & (\kappa_1-\kappa_2)(\cos\omega)(\sin\omega) \\ (\kappa_1-\kappa_2)(\cos\omega)(\sin\omega)\kappa_2(\cos\omega)^2 + \kappa_1(\sin\omega)^2 \end{bmatrix} \quad (10)$$

$$k_{\text{eff, copper}} = \begin{bmatrix} k_2(\sin\omega)^2 + k_1(\cos\omega)^2 & (k_1-k_2)(\sin\omega)(\cos\omega) \\ (k_1-k_2)(\sin\omega)(\cos\omega)k_2(\cos\omega)^2 + k_1(\sin\omega)^2 \end{bmatrix} \quad (11)$$

The symbols k_m and κ_m represent the mean thermal conductivity and permeability values in copper MF, calculated as per references [51–53], while σ shows the anisotropy factor, with *Kn = 0* indicating an isotropic MF. For copper MF, its thermal conductivity and permeability are determined by formulas $k_1 = (1 + Kn) \times k_m$ and $k_2 = (1 - Kn) \times k_m$. In a parallel manner, permeability values are given by $\kappa_1 = (1 - Kn) \times \kappa m$, $\kappa_2 = (1 + Kn) \times \kappa_m$. Furthermore, in computing the thermophysical properties in the mushy region, a linear weight average approach was applied.

As the anisotropic factor needs to be kept at a reasonable level to ensure the MF's continuity, the MF's average permeability (κ_a) and effective thermal conductivity (k_a) were established, drawing on previous studies [45,48,54]:

$$\kappa_a = \left(\frac{\varepsilon d_{fp} \sqrt{\frac{\kappa_{tor}}{3\varepsilon}}}{6} \right)^2 \frac{1}{(\kappa_{tor} - 1)\kappa_{tor}} \tag{12}$$

$$k_a = \frac{1}{3}(1 - \varepsilon)k_{copper} \tag{13}$$

Consideration of extra equations involving κ_{tor} and d_{fs} is necessary. These help in establishing k_{copper}, pores per inch (PPI) property (d_{fp}), and the bulk thermal conductivity of the MF material as [54]:

$$\frac{1}{\kappa_{tor}} = \frac{3}{4\varepsilon} + \frac{\sqrt{9 - 8\varepsilon}}{2\varepsilon} \cos\left\{ \frac{4\pi}{3} + \frac{1}{3} \cos^{-1}\left(\frac{8\varepsilon^2 - 36\varepsilon + 27}{(9 - 8\varepsilon)^{\frac{3}{2}}} \right) \right\} d_{fp} \tag{14}$$

$$\frac{d_{fs}}{d_{fp}} = \left(\frac{59}{50} \right) \left(\frac{1 - \varepsilon}{3\pi} \right)^{\frac{1}{2}} \left[1 - \exp\left(\frac{\varepsilon - 1}{0.04} \right) \right]^{-1} \tag{15}$$

$$d_{fp} = \frac{25.4}{PPI} \times 10^{-3} \tag{16}$$

The evaluation involved determining the Frochheimer parameter (C_F) as follows [54]:

$$C_F = \left(\frac{1}{1 - \varepsilon} \right)^{0.132} \left(\frac{d_{fp}}{d_{fs}} \right)^{1.63} 2.12 \times 10^{-3} \tag{17}$$

The provided equation, characterized as an integral ratio, is used for calculating the melting volume fraction (MVF). This non-dimensional value quantitatively expresses the average portion of PCM that has transitioned into a melted state.

$$MVF = \frac{\oint_V (\varepsilon\varphi) dV}{\oint_V (\varepsilon) dV} \tag{18}$$

The power of energy storage is determined by the volume of energy that is amassed over a given time period, measured by the quantity of energy accumulated from the PCM's starting cold phase up to a specific moment in the charging process. The total energy stored, denoted as Q_{store}, is the sum of two distinct types of heat energy.

$$\text{Power} = Q_{\text{store}}/time \tag{19}$$

$$Q_{\text{store}} = Q_{\text{sensible}} + Q_{\text{latent}} \tag{20}$$

$$Q_{sensible} = (T - T_0)(\rho C_P)_{\text{copper}} \oint_V (1 - \varepsilon) dV + \oint_V \left(\int_{T_0}^{T} \varepsilon (\rho C_P)_{wax}(T) dT \right) dV + (T - T_0)(\rho C_P)_{\text{Wall}} V_{\text{Wall}} + (T - T_0)(\rho C_P)_{\text{HTF}} V_{\text{HTF}} \tag{21}$$

$$Q_{latent} = \varepsilon \oint_V (\rho_{wax} \varphi L_{wax}) dV \tag{22}$$

Considering the boundary and initial conditions, zero velocities were assumed at all walls. The hot temperature of the heated wall was considered as T_w = 339.65 K, and the initial super-cold temperature of 324.65 K. A zero relative reference pressure was applied at the top left corner.

The FEM ensures accurate and consistent outputs across the mesh, suitable for this study's goal. Calculation started with initial conditions to examine energy storage and phase transitions. Thermal and continuity equations, along with phase field variables, ϕ,

were solved iteratively. This simulation stopped when MVF reached > 0.99 for melting. Figure 4 shows the computational algorithm used for the simulation of melting progression. Through the FEM, the equations are integrated across elements using Gauss quadrature. The outcome is a collection of algebraic residual equations. These equations are then iteratively solved with the aid of the PARDISO solver [55,56].

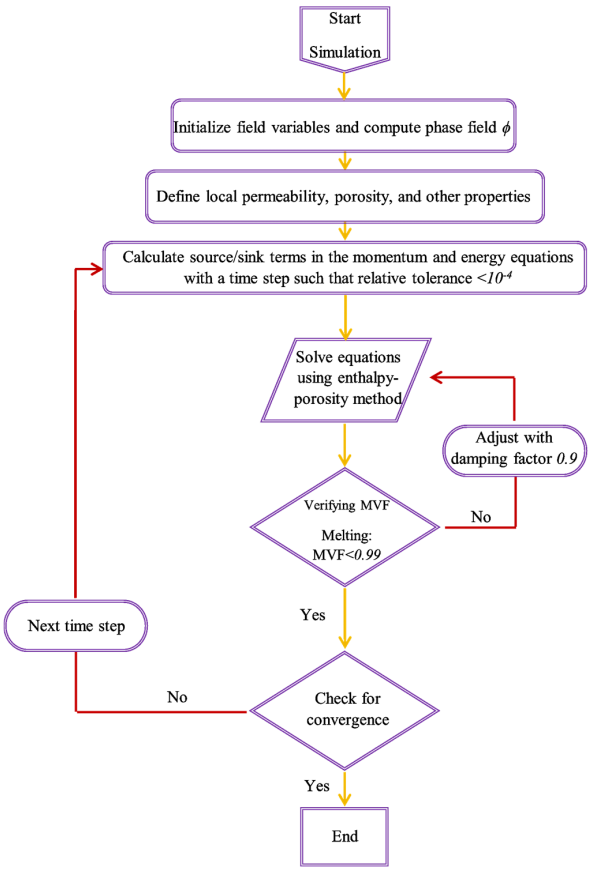

Figure 4. Flowchart of the computational method for solving the governing equations for PCM melting.

Table 1 lists the thermophysical properties of paraffin as a PCM and copper foam as a MF, both key components in a solar heating system's LHTES unit. These materials improve system stability and efficiency in solar energy applications by optimizing heat storage and transfer. The PCM manages energy fluctuations through phase transitions, while the copper foam improves heat exchange across the system.

Table 1. Properties of paraffin as a phase-change material (PCM) and copper foam as a metal foam (MF).

Materials	C_p (J/kg.K)	ρ (kg/m^3)	k (W/m.K)	Melting Point (K)
Paraffin (solid/liquid) [51–53]	2700/2900	916/790	0.21/0.12	324.65
Copper foam [57]	386	8900	380	

3. Mesh Sensitivity Analysis

A thorough evaluation was performed to determine the impact of mesh resolution on computational precision, specifically examining the AMFL at the bottom and top case settings with parameters Kn = 0.2 and ω = 90° during the PCM's melting. The domain was discretized using a structured mesh controlled by the mesh resolution parameter, Nm.

Figure 5 displays the MVF and total heat transfer across various mesh sizes, *Nm* = 6, 7, 8, 9, and 10, during the melting process. Detailed descriptions of the mesh configurations and their respective computational times for complete melting are provided in Table 2. There is a predictable escalation in computational demands as the mesh resolution increases, which is attributed to the rise in the number of quadrilateral and edge elements. The computational load intensifies as the mesh density grows with higher *Nm* values. For instance, *Nm* = 10 sees the melting computational time extend to 86 h and 45 min, while this time is minimized to only 36 h and 6 min for *Nm* = 6. Therefore, for optimal balance between accuracy and computational efficiency, the mesh network at *Nm* = 8 was selected for further computations, as it offers satisfactory precision within a reasonable time frame, totaling 63 h and 42 min.

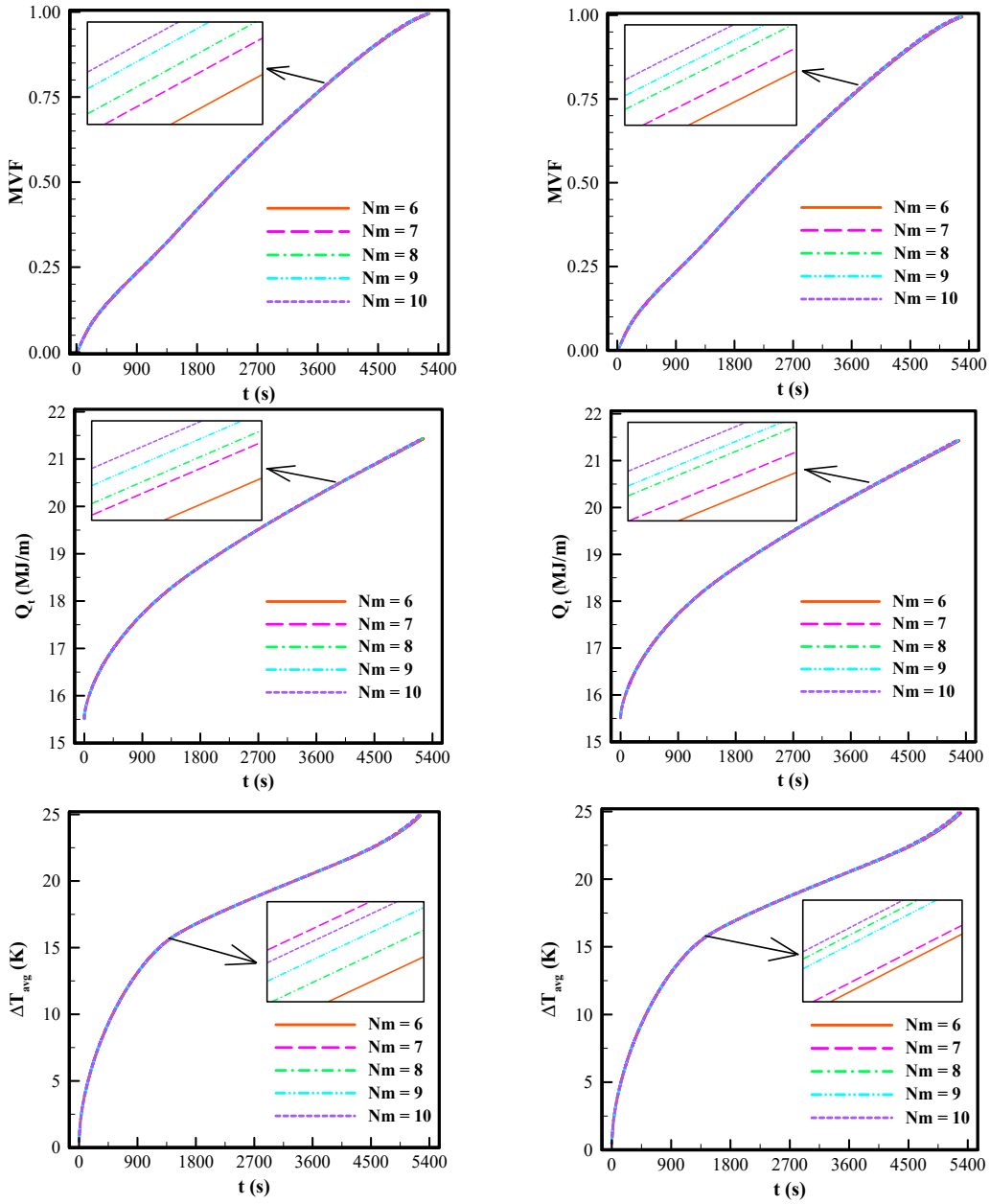

Figure 5. Mesh study. The bottom case is represented on the **left**, and the top case is on the **right**.

Table 2. Run time for different cases of *Nm*.

Nm	Runtime	
	Bottom Case	Top Case
6	36 h 6 min	36 h 6 min
7	49 h 5 min	49 h 4 min
8	63 h 42 min	63 h 42 min
9	81 h 11 min	81 h 11 min
10	86 h 44 min	86 h 45 min

4. Model Verification

In the research conducted by Zheng et al. [57], a composite paraffin PCM-MF was scrutinized both empirically and mathematically within an enclosure measuring 10 × 10 × 3 cm. The research focused on three distinct heating conditions, where heat was applied separately to the left, bottom, and top sections of the composite PCM. Here, the configuration, including the left hot wall, subjected to a heat flux of 1150 W, was deemed as verification, while the other surrounding boundaries of the composite PCM had minimal heat loss. The MF used in the PCM, which featured a high porosity of 0.95 and a density of 5 pores per inch (*PPI*), influenced the thermal dynamics observed during the melting procedure of the paraffin wax. Figure 6 illustrates the average temperature along a vertical path positioned 2.5 cm from the plane where heat is applied. Figure 7 demonstrates the transition from liquid to solid state at different times during the melting progression. The observed structural details, boundary delineations, and temperature profiles in this simulation show a significant correlation with the findings of Zheng et al., as presented in reference [57].

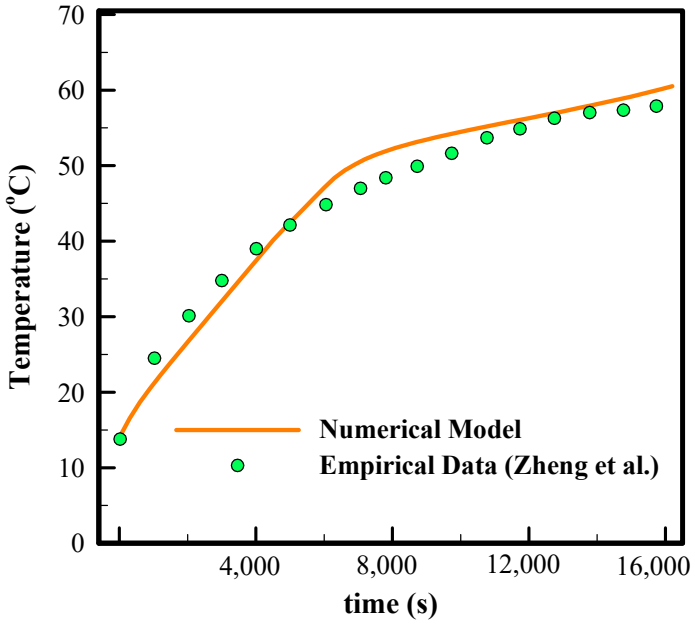

Figure 6. Corroboration of the current study findings via comparative analysis with [57]'s empirical data.

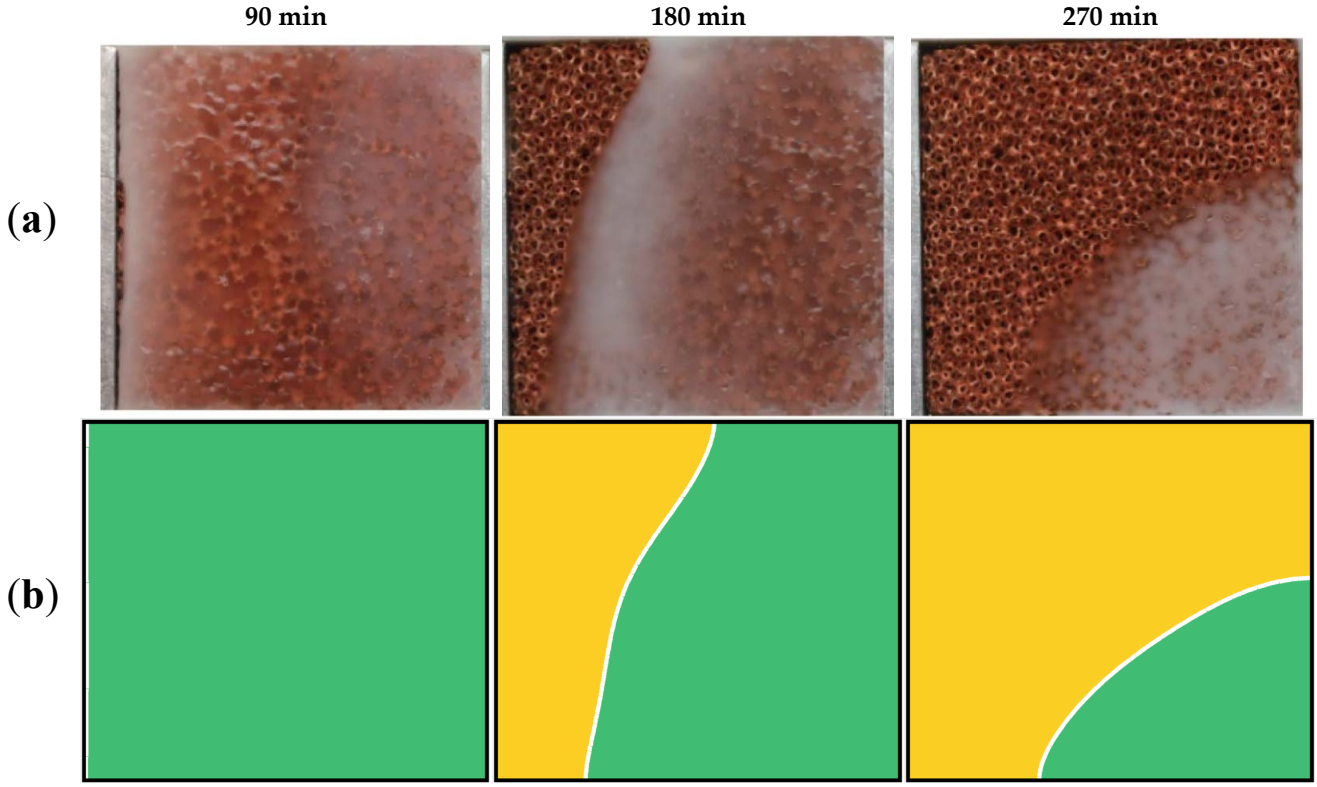

Figure 7. Melting progression of PCM-MF hybrid paraffin in a square cavity: (**a**) empirical data acquired from [57] and (**b**) our latest study outcomes.

5. Results and Discussion

The impact of anisotropy on thermal performance was explored in an LHTES unit containing an AMFL, with the anisotropy angle (ω) ranging from 0° to 90° and an anisotropy parameter set at Kn = 0.1 and 0.2. The system involves water flowing along the walls of the MF within this setup. Three distinct configurations—top, middle, and bottom—were employed to optimize heat transfer and minimize the melting time.

Figures 8–10 provide detailed insights into the top, middle, and bottom cases. Figure 8a indicates the melted volume fraction (MVF), total heat transfer (Q_t), and average temperature difference between the initial and final temperatures (ΔT_{avg}) at a Kn of 0.1. In contrast, Figure 8b exhibits these parameters at a Kn of 0.2. The outcomes suggest that a drop in the anisotropy angle (ω) accelerates the melting progression, enabling the PCM to reach its full energy storage capacity more rapidly, with a growth in the average temperature difference. Importantly, the influence of ω on the melting duration becomes more pronounced at a higher Kn, as shown in Figure 8b. At Kn = 0.2, there is a noticeable fall in the melting transition time as ω approaches zero degrees, from 5659 s at ω = 90° to 4985s at ω = 0°, highlighting the important role of ω in the thermal performance of the system. This is because when ω increases from zero degrees, thermal conductivity begins to weaken in the x direction. Meanwhile, permeability tends to shift to the y direction; hence, convective heat transfer makes headway towards upward movement due to the force of buoyancy. As an illustration, in Figure 8b, at a time of 3600 s (1 h), as the angle shifts from 90° to 0°, the melting rate of the PCM rises by 12.45%, accompanied by an approximately 2.2% upsurge in the total energy stored. A similar trend for MVF and total energy stored was also observed in [58], with heterogeneity parameters valued at 0.1, 0.15, and 0.2, and heterogeneity angles ranging from 0 to 90 degrees.

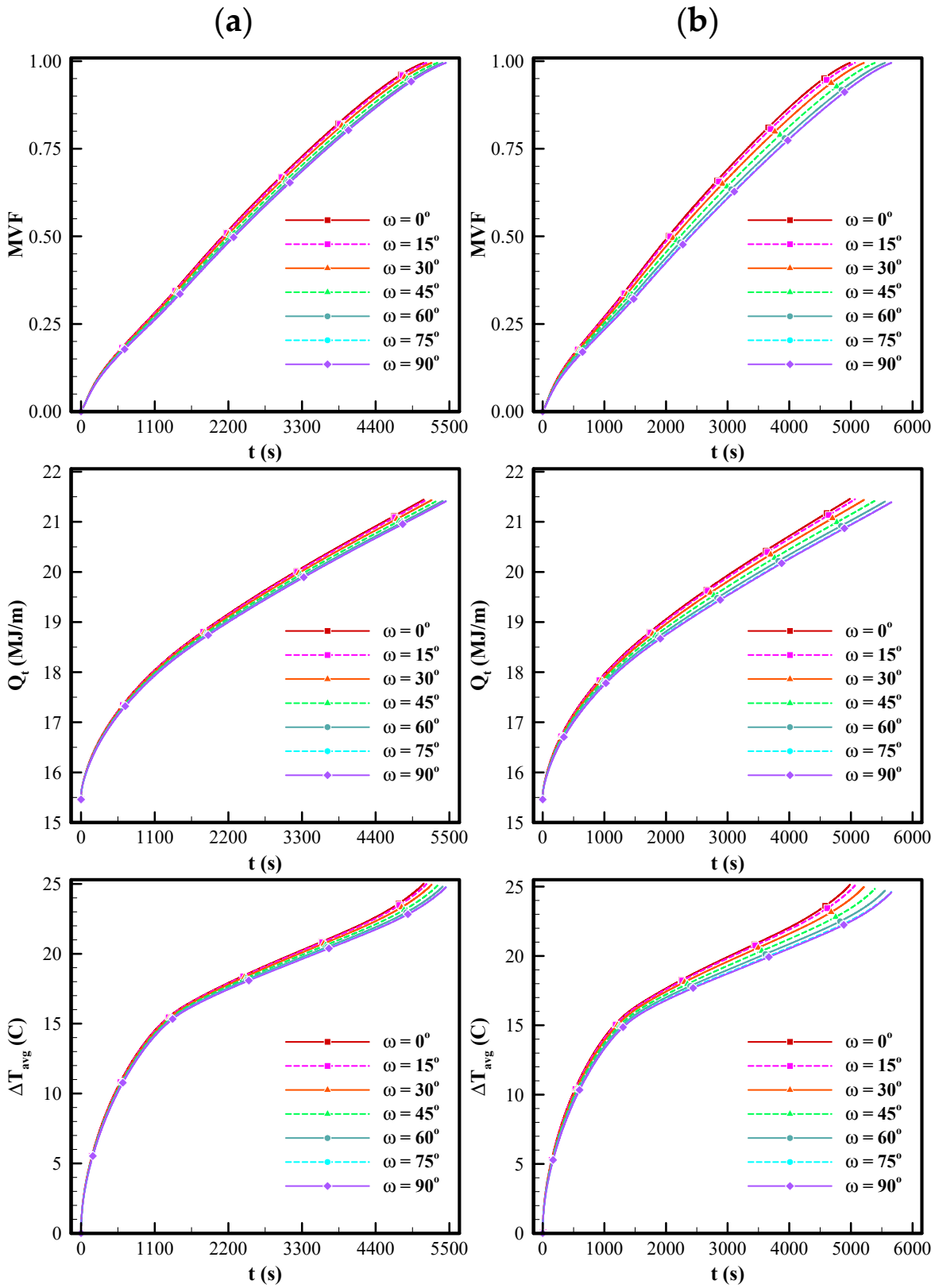

Figure 8. MVF, total heat transfer (Q_t), and average temperature difference (ΔT_{avg}) over the melting progression for the top case at different ω: (**a**) Kn = 0.1 and (**b**) Kn = 0.2.

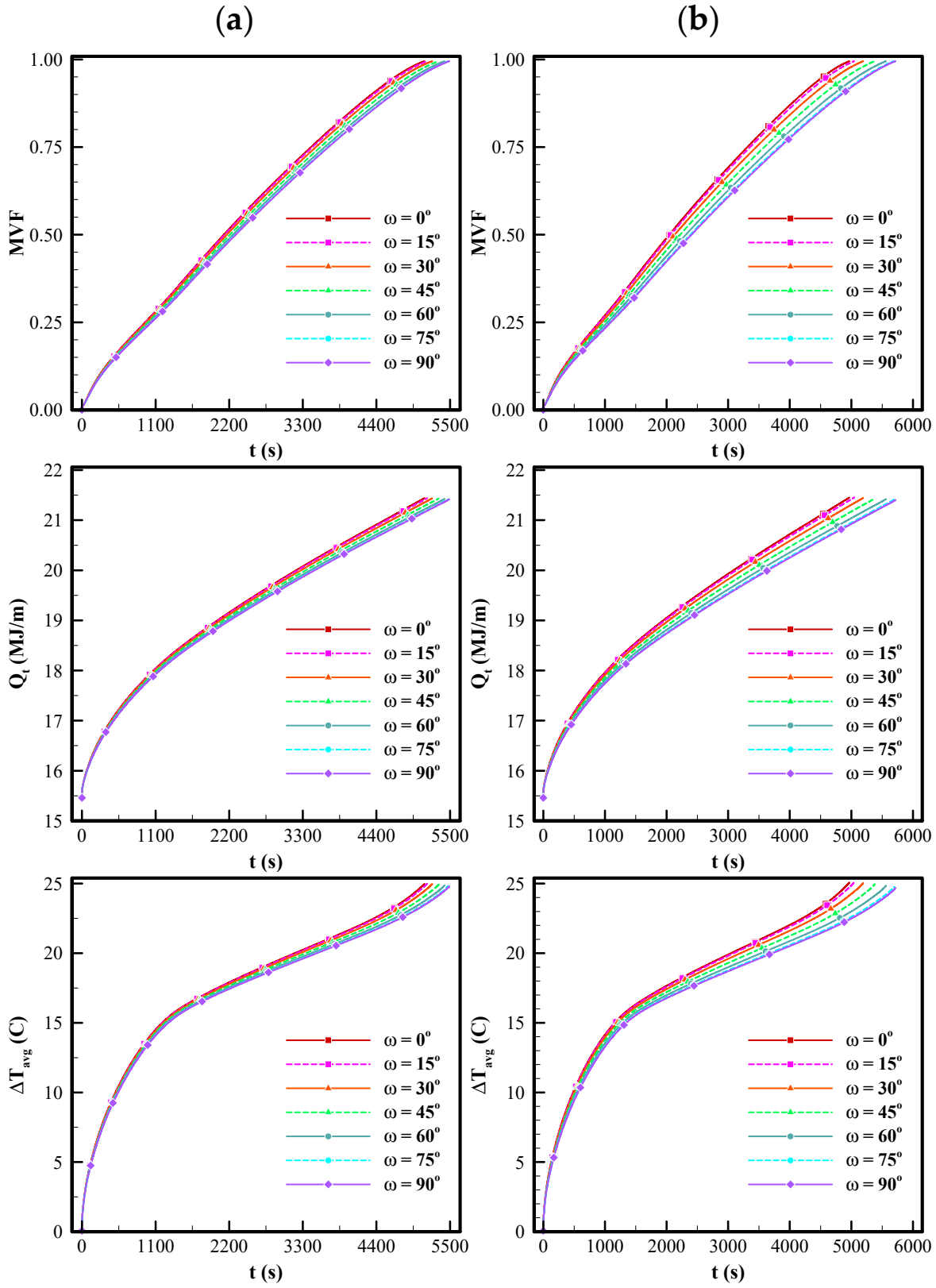

Figure 9. MVF, total heat transfer (Q_t), and average temperature difference (ΔT_{avg}) over the melting progression for the middle case at different ω: (**a**) Kn = 0.1 and (**b**) Kn = 0.2.

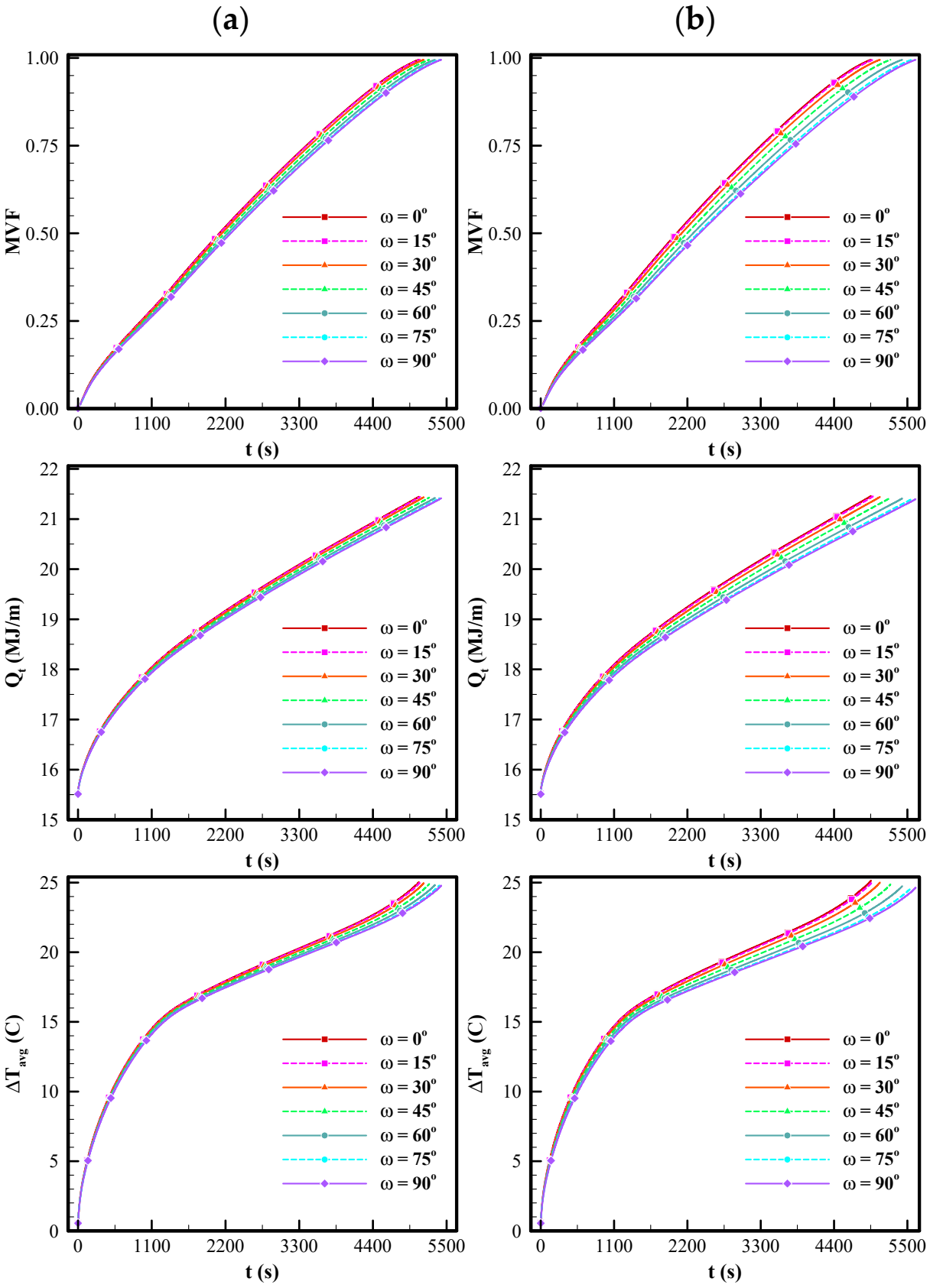

Figure 10. MVF, total heat transfer (Q_t), and average temperature difference (ΔT_{avg}) over the melting progression for the bottom case at different ω: (**a**) Kn = 0.1 and (**b**) Kn = 0.2.

In addition, augmenting the thermal energy stored leads to substantially amplifying the temperature gradient throughout the LHTES unit, from 0 to 25 °C. This escalation is attributed to the system's enhanced capacity to absorb and retain heat energy, primarily facilitated by the PCM employed within the container. The PCM undergoes a physical state transformation from solid to liquid, absorbing a huge amount of heat in the melting process without a corresponding increase in temperature. However, the presence of copper MF ligaments in the cavity prevents the temperature graphs from being at constant temperature. As the energy storage inside the system intensifies, it creates a more pronounced difference in temperature between the initial and final values.

Figure 9 depicts the MVF, total energy stored, and average temperature difference for the middle case. It reveals a modest enhancement in the PCM's melting time attributable to its design, especially for inclinations less than 60 degrees. An evaluation of Figure 9a,b shows the relationship between the *Kn* and its effects on the morphology of MF when infused with PCM, and how these morphological changes influence the PCM's thermal performance. With *Kn* growing, the MF structure becomes more anisotropic, leading to a variation in the ligament thickness: thicker in one direction and thinner in another, orthogonal direction. This modification in MF's structure, linked to higher *Kn* values, directly correlates with improvements in the PCM's melting process, as specifically displayed in Figure 9b for $Kn = 0.2$. In addition, between 0 and 25 °C, the thermal energy storage widens the temperature differential across the LHTES unit. This amelioration is associated with the system's superior heat absorption and retention capacity, largely due to the PCM deployed within. The PCM shifts from solid to liquid, seizing considerable heat in the melting phase with no equivalent uptick in temperature. Yet, including copper MF ligaments inside the unit prevents the temperature from stabilizing throughout the phase-change step.

Figure 10 reveals the same parameters for the bottom configuration, wherein the AMFL is strategically positioned to channel heat towards the right corner of the enclosure effectively. The shift towards a more anisotropic MF structure, driven by the increased *Kn*, is essential for the observed decrease in melting time and the augmented total energy stored. Moreover, the MVF charts emphasize a marked diminution in the time to liquefy attributable to the PCM's tailored design influenced by the Kn, as evidenced in Figure 10b compared to Figure 10a. Therefore, the interplay between *Kn* and the MF's anisotropic morphology is pivotal in optimizing the PCM's performance, accentuating the bottom design's efficiency in thermal management applications. The significance of the bottom scenario is further elucidated in the subsequent figure.

Figure 11 casts light on the duration of phase transition across various scenarios. It is evident that a higher ω leads to a prolonged melting process in all of the designs, with those at *Kn* of 0.2 experiencing a sharper increase compared to those at $Kn = 0.1$. Consider the middle design; diminishing ω from 90° to 0° shortens the melting time by 13.12% for $Kn = 0.2$, while for $Kn = 0.1$, the reduction is only 6.75%. Furthermore, it is noteworthy that although designs with a *Kn* of 0.2 benefit from a reduced melting duration at $\omega = 0°$, they witness a longer solid-to-liquid time at $\omega = 90°$ in comparison to configurations at $Kn = 0.1$. Indeed, $\omega = 45°$ presents a critical threshold in the inclination angle; below this angle, all cases with a *Kn* of 0.2 melt the PCM more swiftly than their $Kn = 0.1$ counterparts. Conversely, the reverse is true for angles ranging between 45° and 90°. The explanation is that a rise in ω causes the thermal conductivity of the AMFL to redirect from horizontal to vertical directions, bringing about low thermal conductivity in the x direction because of an impediment to the temperature x-gradient. Thus, in the range from 45° to 90°, the designs with $Kn = 0.1$ outperform their counterparts at $Kn = 0.2$, underscoring the decisive impact of ω on the LHTES unit's heat management.

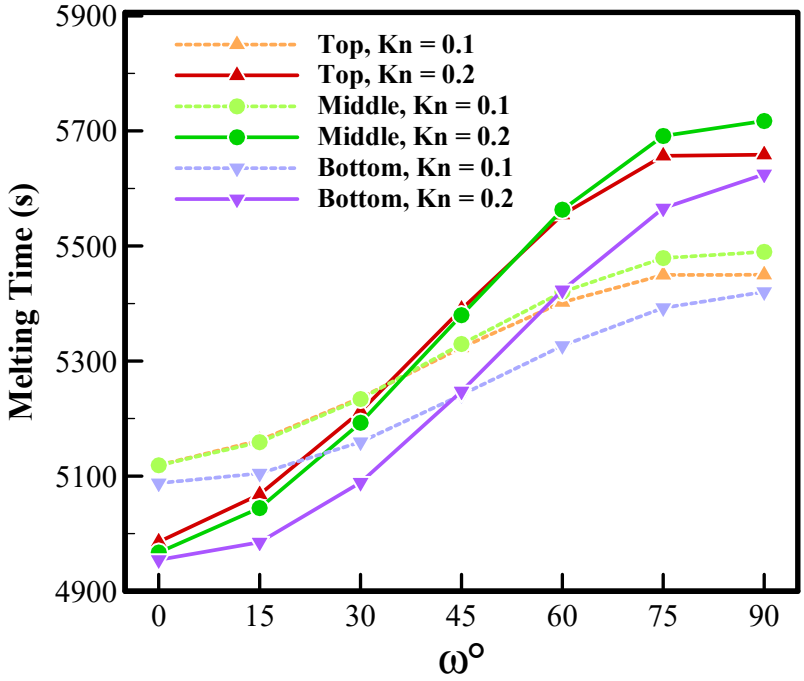

Figure 11. The required melting time for top, middle, and bottom scenarios at various ω and Kn.

When considering a single configuration with a constant ω, altering Kn to a higher value achieves a shorter duration for scenarios with ω below 45°, attributed to the influence of increased Kn on the MF morphology. As Kn rises, the MF becomes more anisotropic, resulting in thicker and thinner ligaments in another orthogonal direction. The ω specifies the orientation of these changes relative to the geometry. However, for ω above 45°, a shift to a higher Kn value while keeping ω constant results in a longer liquefaction period, owing to the strengthened impact of ω, which becomes more influential under these conditions. To compare the effect of Kn on the phase-change duration, while the middle case with ω of 90° has the longest thawing time, at 5717 s, it also exhibits the greatest decrease in time when Kn is shifted from 0.1 to 0.2, resulting in a 4.14% reduction in the melting time.

Moving on to the AMFL position, among the three selected configurations, the largest reduction in phase transition duration is seen in the bottom scenario, where the AMFL facilitates the efficient direction of thermal energy from the heated wall to the lower right corner of the cavity, a location markedly distant from the hot zone. Regarding AMFL placement, the largest difference in melting rate is observed between the top and bottom designs at Kn = 0.2 and ω = 45°. For the aforementioned values, opting for the bottom configuration over the top one results in a 2.72% improvement in liquefaction time, owing to the optimized positioning of the AMFL. Lastly, it is obvious that the melting time for the top and middle configurations exhibits a remarkably similar trend across most angles, except for 75° and 90°, where slight variations become evident.

Figures 12–14 visualize a comparative analysis of the composite PCM-MF behavior at ω = 0° to ω = 90° for the top, middle, and bottom configurations over time intervals: 300 s, 1250 s, 2500 s, 3750 s, and 5000 s, focusing on isotherms and MVF contours.

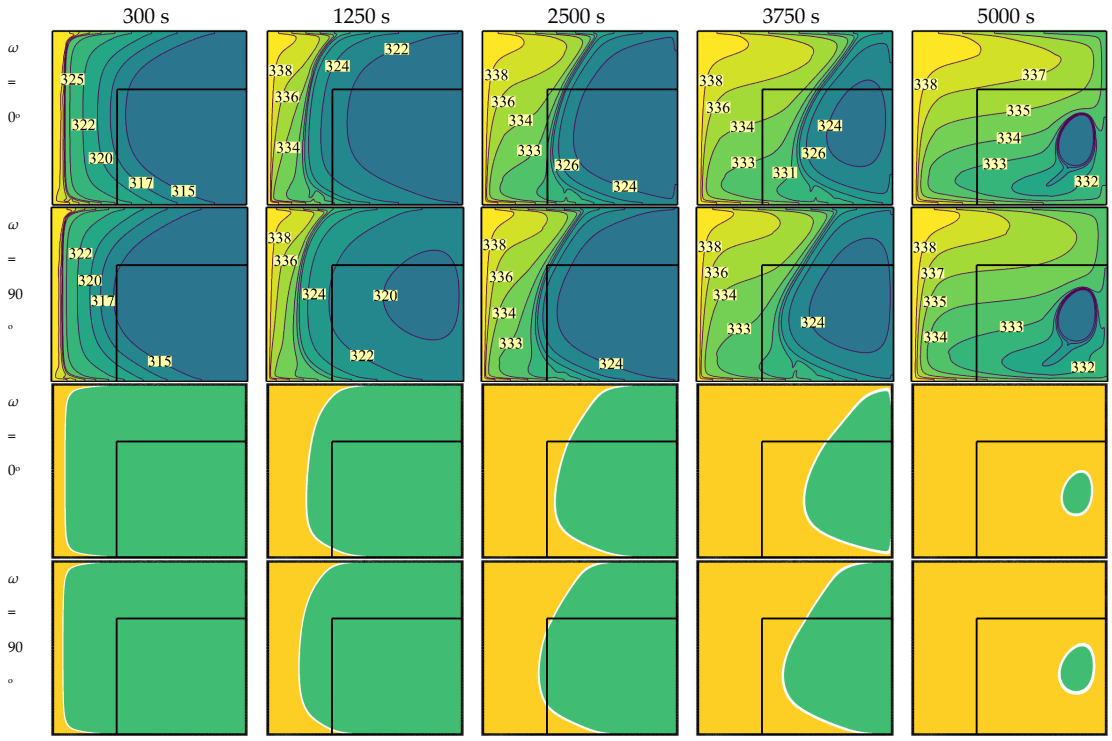

Figure 12. Isotherms and MVF contours for the top case at selected melting time for $\omega = 0°$ and 90° at $Kn = 0.2$. In MVF contours, the yellow area represents the molten PCM, while the green area indicates the solid PCM.

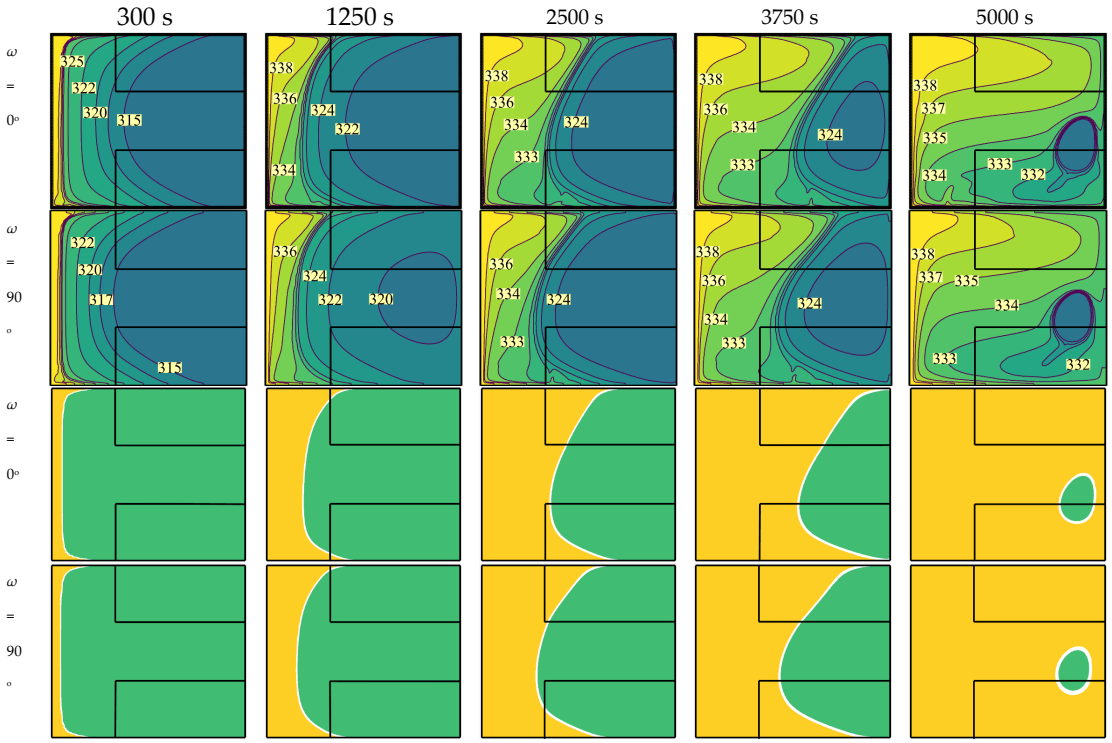

Figure 13. Isotherms and MVF contours for middle case at selected melting time for $\omega = 0°$ and 90° at $Kn = 0.2$. In MVF contours, the yellow area signifies the molten PCM, while the green area shows the solid PCM.

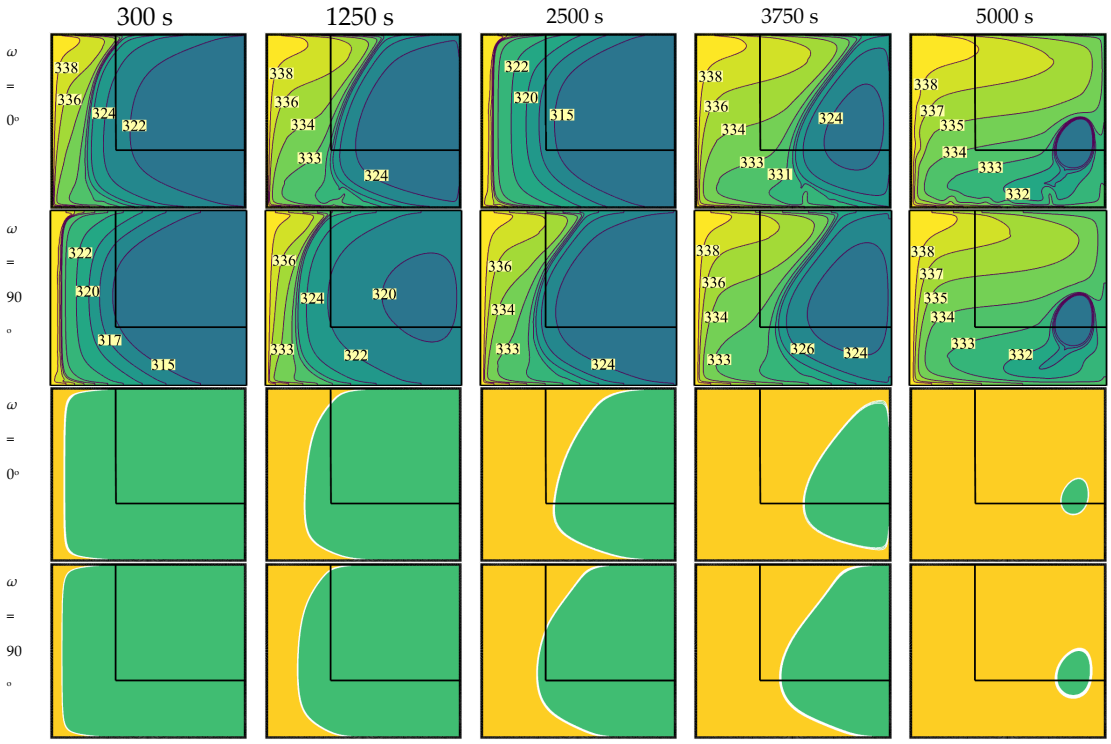

Figure 14. Isotherms and MVF contours for the bottom case at a selected melting time for $\omega = 0°$ and $90°$ at $Kn = 0.2$. In MVF contours, the yellow region depicts the molten phase of PCM, whereas the green region denotes the solid phase.

In the molten PCM, there are two regions warmer than any others: the left area adjacent to the hot wall, and the top area. The heat generated from the hot wall tends to move up and accumulate around the top area because of the buoyancy force and the nature of the upward convection movement. The coexistence of the top design's AMFL and cumulative heat is unfavorable, as shown in Figure 12. At 1250 s, the melting frontier advances with the same pattern for the ω of both $0°$ and $90°$ cases. As time goes by, the effect of ω becomes more noticeable at t = 2500 s, with a bigger extension in AMFL at $\omega = 90°$. More importantly, by t = 3750 s, the melting line at the cavity's top area surpasses the lower at an incredible pace thanks to the free convection as well as the higher thermal conductivity of $\omega = 0°$ in the x direction, resulting in a significant fall in thawing time. Consequently, despite the AMFL's superior heat transfer efficiency, it cannot be deemed the optimal choice when utilized in the top configuration. Tightly clustered temperature lines, particularly evident in the cavity's upper portion, suggest substantial temperature variations across the system. Around the 5000 s mark, the cavity undergoes a great phase change, with a predominant shift towards a fluid phase, displaying temperatures closely resembling those observed at the hot wall.

Figure 13 illustrates the middle case's temperature distribution through isotherms and MVF contours. This design shows the worst thermal performance at ω of $90°$, where thermal conductivity is maximized in the y direction. This observation suggests a critical role for thermal conductivity orientation in determining the system's overall heat transfer efficiency. Although an escalation in ω helps in convection effects due to improved permeability in the y direction, it also lowers thermal conductivity, serving as a dominant mechanism in the x direction, which hampers the growth of the molten zone.

Figure 14 showcases analogous parameters for the bottom configuration contours, demonstrating a notably superior advancement in heat transfer. The temperature distribution illustrates the convective heat transfer and exchange between the solid and molten PCM. As the liquid PCM imparts heat to the solid phase, it descends with minimal temperature gradients. The lower portion of the cavity experiences diminished effectiveness in heat

transfer because of its distance from the high-temperature regions. However, the bottom configuration enjoys the benefits of the optimized design, with AMFL efficiently channeling heat from hot zones to the lower section, distant from the intense temperature gradients. A closer examination of the case with $\omega = 0^\circ$ at a time of 3750 s reveals that the bottom section facilitates a more rapid melting of the PCM compared to other configurations. Conversely, higher ω values delay the time required for melting, observed at t = 5000 s.

6. Conclusions

In this research, the strategic placement of anisotropic and uniform MF layers in an LHTES unit was scrutinized to determine the influence of anisotropy parameters and angles on melting durations. The LHTES unit features three layouts where water, as a heat transfer fluid, circulates through copper MF in a closed square cavity, thermally insulated except for the left heated wall.

The analyses revealed that the bottom design emerged as the most effective configuration, exhibiting the most considerable reduction in phase transition duration. Here, the AMFL's strategic placement directed heat efficiently from the heated wall to the lower right corner of the cavity, markedly distant from the hot zone, resulting in a 2.72% improvement in liquefaction time at $Kn = 0.2$ and $\omega = 45^\circ$ compared to the top configuration. Conversely, the middle case showed the longest thawing time, particularly at a ω of 90°, where the melting time was notably prolonged, reaching up to 5717 s. However, even in this scenario, increasing Kn from 0.1 to 0.2 resulted in a 4.14% reduction in the melting time, demonstrating the beneficial impact of a higher Kn despite the unfavorable angle.

Notably, higher anisotropy angles generally prolonged the melting process across all designs. Specifically, reducing ω from 90° to 0° for the middle design reduced the melting time by 13.12% at $Kn = 0.2$, compared to a reduction of only 6.75% at $Kn = 0.1$, demonstrating the superior performance of higher Kn values in enhancing thermal efficiency. Moreover, the configurations with $Kn = 0.2$ consistently outperformed those with $Kn = 0.1$ at lower ω values, achieving shorter melting durations. This performance advantage is attributed to the increased anisotropy of the MF, which creates thicker ligaments in one direction and thinner ones in another, optimizing heat transfer. However, at higher ω values (above 45°), a shift in the thermal conductivity from the horizontal to vertical direction led to an extended liquefaction period for higher Kn values because of the lowered thermal conduction in the x-axis, highlighting $\omega = 45^\circ$ as a critical angle.

In this study, the enclosure was completely filled with metal foam, allowing for variable configurations of anisotropic layers. The findings indicate that convection behaviors within the anisotropic foam layers significantly affect heat transfer processes, without necessitating additional mass or compromising storage capacity. Future research could explore the use of hybrid systems that combine both anisotropic metal foam and clear flow regions to enhance the impact of anisotropic properties.

Author Contributions: O.Y.: Formal analysis, Funding acquisition, Investigation, Methodology, Resources, Writing—original draft, Writing—review and editing; M.M.: Formal analysis, Conceptualization, Investigation, Methodology, Software, Visualization, Writing—original draft; A.A.: Formal analysis, Investigation, Methodology, Writing—original draft; M.G.: Writing—review and editing, Project administration, Supervision, Conceptualization. Validation. All authors have read and agreed to the published version of the manuscript.

Funding: This project is sponsored by Prince Sattam Bin Abdulaziz University (PSAU) as part of funding for its SDG Roadmap Research Funding Programme, project number PSAU-2023-SDG-55.

Data Availability Statement: The original contributions presented in the study are included in the article, further inquiries can be directed to the corresponding author.

Conflicts of Interest: The authors declare no conflicts of interest.

Nomenclature

Symbol	Unit	Description
Latin		
A_{mush}	kg/(m^{3}s)	mushy constant value in metal foam, 10^{10}
C_F	m	Frochheimer coefficient
C_p	J/(kg.K)	heat capacity per unit of mass
d_{fp}	m	pore diameter
d_{fs}	m	pore characteristics
dV	m	elemental volume
e		porous structure constant
F	N/m^3	body force
g	m/s^2	gravity acceleration
h_{sf}	W/(m.K)	coefficient of interface heat transfer
h_v	W/(m^3.K)	interface heat transfer per volume
k	W/(m.K)	thermal conductivity
Kn		anisotropic coefficient parameter
L	m	enclosure width
Lf	J/kg	latent heat of phase change
Nm		parameter for mesh size
MVF		melt fraction
q	W/m^3	heat rate
Q_{latent}	J	stored energy in the latent form
$Q_{sensible}$	J	stored energy in sensible form
Q_{store}	J	stored energy
x, y	m	coordinate system
t	s	time
T	K	temperature field
Tw	K	wall temperature, 339.65 K
T_{fu}	K	fusion temperature, 324.65 K
u	m/s	x-velocity component
V	m/s	velocity vector
v	m/s	y-velocity component
V	m^3	volume
Greek		
α	m^2/s	thermal diffusivity
β	1/K	volume expansion
ε		porosity
κ	m^2	metal foam's permeability
κ_{tor}		pore flow tortuosity
μ	Pa.s	dynamic viscosity
ρ	kg/m^3	density
σ		dummy parameter
φ		melt fraction
ω	degree	anisotropy angle
Subscripts		
eff		effective property
HTF		heat transfer fluid
copper		metal foam
MFL		metal foam layer
Wall		tube wall
wax		phase-change materials

References

1. Ghosh, D.; Ghose, J.; Datta, P.; Kumari, P.; Paul, S. Strategies for phase change material application in latent heat thermal energy storage enhancement: Status and prospect. *J. Energy Storage* **2022**, *53*, 105179. [CrossRef]
2. Masood, U.; Haggag, M.; Hassan, A.; Laghari, M. A Review of Phase Change Materials as a Heat Storage Medium for Cooling Applications in the Built Environment. *Buildings* **2023**, *13*, 1595. [CrossRef]

3. Madad, A.; Mouhib, T.; Mouhsen, A. Phase change materials for building applications: A thorough review and new perspectives. *Buildings* **2018**, *8*, 63. [CrossRef]
4. Hassan, F.; Jamil, F.; Hussain, A.; Ali, H.M.; Janjua, M.M.; Khushnood, S.; Farhan, M.; Altaf, K.; Said, Z.; Li, C. Recent advancements in latent heat phase change materials and their applications for thermal energy storage and buildings: A state of the art review. *Sustain. Energy Technol. Assess.* **2022**, *49*, 101646. [CrossRef]
5. Lu, B.; Zhang, Y.; Sun, D.; Yuan, Z.; Yang, S. Experimental investigation on thermal behavior of paraffin in a vertical shell and spiral fin tube latent heat thermal energy storage unit. *Appl. Therm. Eng.* **2021**, *187*, 116575. [CrossRef]
6. Wu, J.; Chen, Q.; Zhang, Y.; Sun, K. Phase change material heat transfer enhancement in latent heat thermal energy storage unit with single fin: Comprehensive effect of position and length. *J. Energy Storage* **2021**, *42*, 103101. [CrossRef]
7. Tian, Y.; Liu, X.; Xu, Q.; Luo, Q.; Zheng, H.; Song, C.; Zhu, Z.; Gao, K.; Dang, C.; Wang, H.; et al. Bionic topology optimization of fins for rapid latent heat thermal energy storage. *Appl. Therm. Eng.* **2021**, *194*, 117104. [CrossRef]
8. Tiari, S.; Hockins, A.; Mahdavi, M. Numerical study of a latent heat thermal energy storage system enhanced by varying fin configurations. *Case Stud. Therm. Eng.* **2021**, *25*, 100999. [CrossRef]
9. Selimefendigil, F.; Şirin, C. Energy and exergy analysis of a hybrid photovoltaic/thermal-air collector modified with nano-enhanced latent heat thermal energy storage unit. *J. Energy Storage* **2022**, *45*, 103467. [CrossRef]
10. Sami, S.; Etesami, N. Heat transfer enhancement of microencapsulated phase change material by addition of nanoparticles for a latent heat thermal energy storage system. *Energy Rep.* **2021**, *7*, 4930–4940. [CrossRef]
11. Singh, S.K.; Verma, S.K.; Kumar, R. Thermal performance and behavior analysis of SiO_2, Al_2O_3 and MgO based nano-enhanced phase-changing materials, latent heat thermal energy storage system. *J. Energy Storage* **2022**, *48*, 103977. [CrossRef]
12. Yu, X.; Jiang, R.; Li, Z.; Qian, G.; Wang, B.; Wang, L.; Huang, R. Synergistic improvement of melting rate and heat storage capacity by a rotation-based method for shell-and-tube latent thermal energy storage. *Appl. Therm. Eng.* **2023**, *219*, 119480. [CrossRef]
13. Soltani, H.; Soltani, M.; Karimi, H.; Nathwani, J. Heat transfer enhancement in latent heat thermal energy storage unit using a combination of fins and rotational mechanisms. *Int. J. Heat Mass Transf.* **2021**, *179*, 121667. [CrossRef]
14. Mahdi, J.M.; Lohrasbi, S.; Nsofor, E.C. Hybrid heat transfer enhancement for latent-heat thermal energy storage systems: A review. *Int. J. Heat Mass Transf.* **2019**, *137*, 630–649. [CrossRef]
15. Rolka, P.; Kwidzinski, R.; Przybylinski, T.; Tomaszewski, A. Thermal Characterization of Medium-Temperature Phase Change Materials (PCMs) for Thermal Energy Storage Using the T-History Method. *Materials* **2021**, *14*, 7371. [CrossRef] [PubMed]
16. Chen, T.; Liu, S.; Khan, S.Y.; Shen, Y.; Zhang, S.; Wang, Y.; Kumar, M.; Li, Y.; Li, X. Investigation and optimal design of partially encapsulated metal foam in a latent heat storage unit for buildings. *J. Energy Storage* **2024**, *84*, 110979. [CrossRef]
17. Said, M.A.; Hosseinzadeh, K.; Bahlekeh, A.; Rahbari, A.; Tiji, M.E.; Mahdi, J.M.; Cairns, A.; Talebizadehsardari, P. Accelerated charging dynamics in shell-and-multi-tube latent heat storage systems for building applications. *J. Energy Storage* **2024**, *81*, 110286. [CrossRef]
18. Boujelbene, M.; Mahdi, J.M.; Sultan, H.S.; Homod, R.Z.; Yvaz, A.; Chatroudi, I.S.; Talebizadehsardari, P. The potential of arc-shaped fins for expedited solidification in triplex-tube latent heat storage: Parametric investigation. *J. Build. Eng.* **2024**, *82*, 108176. [CrossRef]
19. Kaboré, A.; Tala, J.V.S.; Younsi, Z.; Bougeard, D. Numerical analysis and optimization of the heat transfer enhancement from the heat transfer fluid side in a shell-and-tube latent heat thermal energy storage unit: Application to buildings thermal comfort improvement. *J. Energy Storage* **2023**, *74*, 109530. [CrossRef]
20. M'hamdi, Y.; Bourzik, O.; Baba, K.; Tajayouti, M.; Nounah, A. Parametric Analysis of the Use of PCM in Building Energy Performance. In *Recent Advances in Environmental Science from the Euro-Mediterranean and Surrounding Regions*, 3rd ed.; Springer Nature: Cham, Switzerland, 2024.
21. Xu, Y.; Zheng, Z.-J.; Chen, S.; Cai, X.; Yang, C. Parameter analysis and fast prediction of the optimum eccentricity for a latent heat thermal energy storage unit with phase change material enhanced by porous medium. *Appl. Therm. Eng.* **2021**, *186*, 116485. [CrossRef]
22. Yang, C.; Xu, Y.; Cai, X.; Zheng, Z.-J. Melting behavior of the latent heat thermal energy storage unit with fins and graded metal foam. *Appl. Therm. Eng.* **2021**, *198*, 117462. [CrossRef]
23. Huang, Z.; Zhang, H.; Zhang, C.; Tang, W.; Xiao, G.; Du, Y. A Pore Scale Study on Heat Transfer Characteristics of Integrated Thermal Protection Structures with Phase Change Material. *Energies* **2024**, *17*, 465. [CrossRef]
24. Iasiello, M.; Mameli, M.; Filippeschi, S.; Bianco, N. Metal foam/PCM melting evolution analysis: Orientation and morphology effects. *Appl. Therm. Eng.* **2021**, *187*, 116572. [CrossRef]
25. Chibani, A.; Merouani, S.; Benmoussa, F. Computational analysis of the melting process of Phase change material-metal foam-based latent thermal energy storage unit: The heat exchanger configuration. *J. Energy Storage* **2021**, *42*, 103071. [CrossRef]
26. Yang, C.; Xu, Y.; Cai, X.; Zheng, Z.-J. Effect of the circumferential and radial graded metal foam on horizontal shell-and-tube latent heat thermal energy storage unit. *Sol. Energy* **2021**, *226*, 225–235. [CrossRef]
27. Ren, Q.; Wang, Z.; Lai, T.; Zhang, J.F.; Qu, Z.G. Conjugate heat transfer in anisotropic woven metal fiber-phase change material composite. *Appl. Therm. Eng.* **2021**, *189*, 116618. [CrossRef]
28. Liu, X.; Wang, H.; Xu, Q.; Luo, Q.; Song, Y.; Tian, Y.; Chen, M.; Xuan, Y.; Jin, Y.; Jia, Y.; et al. High thermal conductivity and high energy density compatible latent heat thermal energy storage enabled by porous AlN ceramics composites. *Int. J. Heat Mass Transf.* **2021**, *175*, 121405. [CrossRef]

29. Said, M.A.; Togun, H.; Abed, A.M.; Biswas, N.; Mohammed, H.I.; Sultan, H.S.; Mahdi, J.M.; Talebizadehsardari, P. Evaluation of wavy wall configurations for accelerated heat recovery in triplex-tube energy storage units for building heating applications. *J. Build. Eng.* **2024**, *94*, 109762. [CrossRef]
30. Liang, L.; Diao, Y.H.; Zhao, Y.H.; Wang, Z.Y.; Chen, C.Q. Experimental and numerical investigations of latent thermal energy storage using combined flat micro-heat pipe array–metal foam configuration: Simultaneous charging and discharging. *Renew. Energy* **2021**, *171*, 416–430. [CrossRef]
31. Lei, J.; Tian, Y.; Zhou, D.; Ye, W.; Huang, Y.; Zhang, Y. Heat transfer enhancement in latent heat thermal energy storage using copper foams with varying porosity. *Sol. Energy* **2021**, *221*, 75–86. [CrossRef]
32. Joshi, V.; Rathod, M.K. Experimental and numerical assessments of thermal transport in fins and metal foam infused latent heat thermal energy storage systems: A comparative evaluation. *Appl. Therm. Eng.* **2020**, *178*, 115518. [CrossRef]
33. Nedjem, K.; Teggar, M.; Hadibi, T.; Arıcı, M.; Yıldız, Ç.; Ismail, K.A.R. Hybrid thermal performance enhancement of shell and tube latent heat thermal energy storage using nano-additives and metal foam. *J. Energy Storage* **2021**, *44*, 103347. [CrossRef]
34. Ghalambaz, M.; Aljaghtham, M.; Chamkha, A.J.; Fteiti, M.; Abdullah, A. Latent heat thermal energy storage in a shell-tube: A wavy partial layer of metal foam over tubes. *J. Energy Storage* **2023**, *59*, 106493. [CrossRef]
35. Shen, S.; Zhou, H.; Du, Y.; Huo, Y.; Rao, Z. Investigation on latent heat energy storage using phase change material enhanced by gradient-porosity metal foam. *Appl. Therm. Eng.* **2024**, *236*, 121760. [CrossRef]
36. Shen, Y.; Liu, S.; Jin, H.; Rehman Mazhar, A.; Zhang, S.; Chen, T.; Wang, Y. Thermal investigation and parametric analysis of cascaded latent heat storage system enhanced by porous media. *Appl. Therm. Eng.* **2024**, *238*, 121982. [CrossRef]
37. Zhang, S.; Li, Z.; Yan, Y.; Alston, M.; Tian, L. Comparative study on heat transfer enhancement of metal foam and fins in a shell-and-tube latent heat thermal energy storage unit. *Energy Storage Sav.* **2023**, *2*, 487–494. [CrossRef]
38. Jaisatia Varthani, A.; Shasthri, S.; Baljit, S.; Kausalyah, V. A systematic review of metal foam and heat pipe enhancement in Latent Heat Thermal Energy Storage system. *J. Energy Storage* **2022**, *56*, 105888. [CrossRef]
39. Opolot, M.; Zhao, C.; Liu, M.; Mancin, S.; Bruno, F.; Hooman, K. A review of high temperature ($\geq$500 °C) latent heat thermal energy storage. *Renew. Sustain. Energy Rev.* **2022**, *160*, 112293. [CrossRef]
40. Shank, K.; Tiari, S. A Review on Active Heat Transfer Enhancement Techniques within Latent Heat Thermal Energy Storage Systems. *Energies* **2023**, *16*, 4165. [CrossRef]
41. Tofani, K.; Tiari, S. Nano-Enhanced Phase Change Materials in Latent Heat Thermal Energy Storage Systems: A Review. *Energies* **2021**, *14*, 3821. [CrossRef]
42. Zhang, S.; Mancin, S.; Pu, L. A review and prospective of fin design to improve heat transfer performance of latent thermal energy storage. *J. Energy Storage* **2023**, *62*, 106825. [CrossRef]
43. Bianco, N.; Fragnito, A.; Iasiello, M.; Mauro, G.M. Multiscale analysis of a seasonal latent thermal energy storage with solar collectors for a single-family building. *Therm. Sci. Eng. Prog.* **2024**, *50*, 102538. [CrossRef]
44. Yousefi, E.; Nejad, A.A.; Rezania, A. Higher power output in thermoelectric generator integrated with phase change material and metal foams under transient boundary condition. *Energy* **2022**, *256*, 124644. [CrossRef]
45. Zhang, S.; Yao, Y.; Jin, Y.; Shang, Z.; Yan, Y. Heat transfer characteristics of ceramic foam/molten salt composite phase change material (CPCM) for medium-temperature thermal energy storage. *Int. J. Heat Mass Transf.* **2022**, *196*, 123262. [CrossRef]
46. Ghalambaz, M.; Melaibari, A.A.; Chamkha, A.J.; Younis, O.; Sheremet, M. Phase change heat transfer and energy storage in a wavy-tube thermal storage unit filled with a nano-enhanced phase change material and metal foams. *J. Energy Storage* **2022**, *54*, 105277. [CrossRef]
47. Nield, D.A.; Bejan, A. *Convection in Porous Media*; Springer: Berlin/Heidelberg, Germany, 2006; Volume 3.
48. Yao, Y.; Wu, H. Interfacial heat transfer in metal foam porous media (MFPM) under steady thermal conduction condition and extension of Lemlich foam conductivity theory. *Int. J. Heat Mass Transf.* **2021**, *169*, 120974. [CrossRef]
49. Zhao, C.; Wang, J.; Sun, Y.; He, S.; Hooman, K. Fin design optimization to enhance PCM melting rate inside a rectangular enclosure. *Appl. Energy* **2022**, *321*, 119368. [CrossRef]
50. Ghalambaz, M.; Aljaghtham, M.; Chamkha, A.J.; Abdullah, A.; Alshehri, A.; Ghalambaz, M. An anisotropic metal foam design for improved latent heat thermal energy storage in a tilted enclosure. *Int. J. Mech. Sci.* **2022**, *238*, 107830. [CrossRef]
51. Korti, A.I.N.; Guellil, H. Experimental study of the effect of inclination angle on the paraffin melting process in a square cavity. *J. Energy Storage* **2020**, *32*, 101726. [CrossRef]
52. Agarwal, A.; Sarviya, R. Characterization of commercial grade paraffin wax as latent heat storage material for solar dryers. *Mater. Today Proc.* **2017**, *4*, 779–789. [CrossRef]
53. Ukrainczyk, N.; Kurajica, S.; Šipušić, J. Thermophysical comparison of five commercial paraffin waxes as latent heat storage materials. *Chem. Biochem. Eng. Q.* **2010**, *24*, 129–137.
54. Yao, Y.; Wu, H. Macroscale modeling of solid–liquid phase change in metal foam/paraffin composite: Effects of paraffin density treatment, thermal dispersion, and interstitial heat transfer. *J. Therm. Sci. Eng. Appl.* **2021**, *13*, 041024. [CrossRef]
55. Bollhöfer, M.; Schenk, O.; Janalik, R.; Hamm, S.; Gullapalli, K. State-of-the-art sparse direct solvers. In *Parallel Algorithms in Computational Science and Engineering*; Springer: Berlin/Heidelberg, Germany, 2020; pp. 3–33.
56. Bollhöfer, M.; Eftekhari, A.; Scheidegger, S.; Schenk, O. Large-scale sparse inverse covariance matrix estimation. *SIAM J. Sci. Comput.* **2019**, *41*, A380–A401. [CrossRef]

57. Zheng, H.; Wang, C.; Liu, Q.; Tian, Z.; Fan, X. Thermal performance of copper foam/paraffin composite phase change material. *Energy Convers. Manag.* **2018**, *157*, 372–381. [CrossRef]
58. Ghalambaz, M.; Aljaghtham, M.; Chamkha, A.J.; Abdullah, A.; Mansir, I.; Ghalambaz, M. Mathematical modeling of heterogeneous metal foams for phase-change heat transfer enhancement of latent heat thermal energy storage units. *Appl. Math. Model.* **2023**, *115*, 398–413. [CrossRef]